Influence of Thermochemical Modelling of CO_2-N_2 Mixtures on the Shock Interaction Patterns at Hypersonic Regimes

Catarina Garbacz * and Fábio Morgado † and Marco Fossati ‡
Aerospace Centre of Excellence, University of Strathclyde, Glasgow, G1 1XJ, United Kingdom

Michele Capriati § and Thierry Magin ¶
von Karman Institute for Fluid Dynamics, Rhode-Saint-Genese, 1640, Belgium

The effect of finite-rate internal energy transfer on shock interaction mechanisms of CO_2-dominated flows is investigated. The polyatomic molecule has a relatively low characteristic vibrational temperature that causes vibrational degrees of freedom to be excited across a shock wave at hypersonic regimes. In this paper, the impact of accounting for the time associated to the relaxation of this process, as opposed to assuming instant thermal equilibrium, on the shock structures occurring in the flowfield over a double-wedge geometry is numerically studied. A Mach 9 flow over two different geometries is simulated with two different models, the two-temperature model of Park and the thermally perfect gas model. Simulations are carried out with the SU2 software that is coupled to the Mutation++ library, providing thermodynamic, chemical kinetic and transport properties of any mixture of gases for a given state of the flow. Anisotropic mesh adaption is used with the AMG library to accurately capture highly directional and high-gradient localized flow features. Results show that different ways of modelling the effect of vibrational relaxation have a major impact on the size of the compression corner separation bubble, leading to different shock wave systems in this region. As a consequence, the obtained shock interaction mechanisms differ as well. The shock patterns obtained for the thermally perfect gas model result in stronger impingement on the surface and higher aerodynamic loads of pressure and heat flux.

I. Introduction

DURING atmospheric reentry or sustained hypersonic flight, the most severe aerothermal loads acting on the surface of the vehicle can arise from interference phenomena between shock waves. It is common for this interference to result in shock impingement which, in turn, leads to very high localized peaks in surface pressure and heat flux. The accurate prediction of shock interaction flow patterns is therefore a key element in aerodynamic design of space vehicles.

The first systematic study on the topic was conducted by Edney [1], and his work consisted of experimentally impinging an oblique shock on a bow shock in front of a cylinder. Depending on the angle of the oblique shock and, consequently, the location of the intersection, distinct shock interference patterns were identified and classified into six different shock interaction types using a shock-polar approach. This pioneer classification has since then been used in subsequent works by other authors, not only in the case of a cylinder oblique/bow shock interaction, but also in the case of a flow over a double-wedge geometry, as considered in this paper. The latter is particularly relevant for design since it is found inside the propulsive system of space vehicles and it also represents regions in the proximity of control surfaces and/or the fuselage-canopy area. For an in-depth understanding of the different shock structures and transitions between them, initial works focused exclusively on doing numerical simulation of inviscid flow [2–5]. Characteristics of viscous/inviscid interaction, including shock wave/boundary layer interaction, were also explored numerically and experimentally [6–8]. Overall it was concluded that viscosity effects have an impact on the interaction transition points, and trigger more complex flow features such as separations shocks, reattachment shocks, shear layer unsteadiness and interactions among them. Furthermore, surface pressure distributions differed significantly between viscous and inviscid simulations [7]. All the previous studies assumed a flow of air behaving as a perfect ideal gas

*PhD student, Department Mechanical and Aerospace Engineering, AIAA Member.
†PhD student, Department Mechanical and Aerospace Engineering, AIAA Member.
‡Lecturer, Department Mechanical and Aerospace Engineering, AIAA Member.
§PhD student, Department of Aeronautics and Aerospace.
¶Associate Professor, Department of Aeronautics and Aerospace, AIAA Member.

(specific heat ratio $\gamma = 1.4$). However, at hypersonic regimes, high-temperature effects such as molecular vibrational excitation and chemical dissociation play a part in the gas dynamics and should not be neglected. By comparing to a perfect ideal gas model, Tchuen et al. [9, 10] have shown numerically that nonequilibrium gas effects significantly alter the structure of the shock interaction and the surface pressure distribution in air flows.

With recent space programs for missions to Mars, the research community has raised interest in its atmosphere, consisting of a carbon-dioxide-dominated gas. The molecular structure of this triatomic molecule differs from the diatomic ones encountered in air (N_2, O_2) in terms of behaviour of the vibrational degrees of freedom and subsequent energy redistribution among the various internal modes. This results in a characteristic vibrational temperature that is lower than in the case of air, with a non-negligible impact on the nonequilibrium processes. Candler [11] studied a Martian atmospheric entry flow of CO_2-N_2 and has shown that, due to the very fast vibrational relaxation of CO_2, there is very little thermal nonequilibrium. The two-temperature nonequilibrium model for CO_2 was developed by Park [12]. By applying the model to a reentry simulation stagnation-line flow, the conclusions drawn by Candler were confirmed.

Despite the extensive work done on CO_2 hypersonic flows and its nonequilibrium physics, the literature discussing shock interaction patterns for this gas mixture is scarce to the best of the authors' knowledge. Windisch et al. [13] simulated the impingement of an oblique shock on a bow shock in front of a cylinder in a CO2-dominated flow, from which a type VII interaction pattern was obtained. A comparison with the same test-case but considering instead an N_2 mixture revealed that the post-shock temperatures were significantly lower for the gas model of the Martian atmosphere, resulting in a higher fluid density and a much smaller shock stand-off distance. Morever, regions of thermal nonequilibrium were very small, due to the fast vibrational relaxation. Recent studies conducted by the authors of this paper [14] compared shock interaction patterns resulting from an inviscid Mach 9 flow over a double-wedge, for air and CO_2 mixtures. Numerical results lead to two important conclusions: 1) for lower freestream temperatures, the nonequilibrium shock interaction patterns differ between air and CO_2 flow, with a large impact on the surface pressure distribution, 2) a comparison with a perfect ideal gas model revealed that, despite the small degree thermal nonequilibrium encountered in the case of CO_2, it still has a significant impact on the obtained interaction pattern and therefore vibrational excitation should be accounted for.

In this work the authors aim at extending the previous study to include viscous effects and understand shock/shock and shock/boundary later interaction patterns in more realistic CO_2-dominated flows. Moreover, the paper will focus on comparing two different ways of modelling vibrational energy relaxation and assessing the impact of these models on the identified flow features and regions of the vehicle's surface that may be subjected to peaks of pressure and heat flux. The more complete two-temperature model by Park [12] assumes that the vibrational modes may relax considerably slower than the rate of fluid motion, therefore considering a separate vibrational temperature of the mixture; the thermally perfect gas model will be used to implicitly account for vibrational excitation by having thermodynamic properties such as specific heats changing accordingly with temperature and considering one temperature only. To this purpose, a Mach 9 viscous flow over a 15°-40°and a 15°-50°double-wedge is simulated. A CO_2-N_2 mixture model is used to mimic the Martian atmosphere. Simulations are performed with the open-source CFD code SU2 [15], with the specific branch SU2-NEMO [14] dedicated to the study of hypersonic flows with high-temperature effects. The complexity of these type of flows typically results in regions of nearly-uniform flow properties separated by very localized and very high-gradient flow features such as shock waves, contact discontinuities and boundary layers. To ensure that all these features are accurately captured at an affordable computational cost, automatic mesh adaptation is used as a means to achieve this compromise. The paper is organized as follows: Section II introduces the governing equations and physical models; Section III gives an overview of the numerical tools and methods; Section IV presents the simulated test-cases, a grid-convergence study and numerical results for assessing the influence of the vibrational relaxation model on the shock interaction patterns; finally in Section V the main conclusions are drawn.

II. Physical Modelling

A. Nonequilibrium models (NEQ)

The system of governing equations implemented with the nonequilibrium models follows the Navier-Stokes approach presented in the literature for a continuum, viscous laminar, chemically-reacting, thermal nonequilibrium flow [16]. The two-temperature model by Park is used to model thermal nonequilibrium. It has been developed initially for air [17] but later modified for CO_2 flows [12] and validated in refs. [18, 19] against experimental data and the more detailed state-to-state approach, respectively. The model assumes that rotational relaxation is very fast relative to the rate of fluid motion and therefore considers that the translational and rotational modes of the gas are in equilibrium with each

other at the translational-rotational temperature T_{tr}. As for vibrational relaxation, the CO_2 triatomic molecule has three vibrational modes, one of which is double degenerate. Camac [20] showed that all three modes relax at the same time, but considerably slower than the rate of fluid motion, leading to a single separate temperature to describe this process. Electronic modes are assumed to be at equilibrium with vibration, therefore it is considered that these two modes relax at the vibro-electronic temperature T_{ve}. In a compact form, the system of equations can be described as

$$\frac{\mathrm{d}\mathbf{U}}{\mathrm{d}t} + \nabla \cdot \vec{\mathbf{F}}^{\mathrm{c}}(\mathbf{U}) = \nabla \cdot \vec{\mathbf{F}}^{\mathrm{v}}(\mathbf{U}) + \mathbf{Q}(\mathbf{U}) \tag{1}$$

where the conservative variables, convective fluxes, viscous fluxes, and source terms are given by

$$\mathbf{U} = \begin{Bmatrix} \rho_1 \\ \dots \\ \rho_{n_s} \\ \rho\vec{u} \\ \rho e \\ \rho e^{\mathrm{ve}} \end{Bmatrix}, \quad \vec{\mathbf{F}}^{\mathrm{c}} = \begin{Bmatrix} \rho_1\vec{u} \\ \dots \\ \rho_{n_s}\vec{u} \\ \rho\vec{u}\otimes\vec{u} + p\bar{I} \\ \rho h\vec{u} \\ \rho e^{\mathrm{ve}}\vec{u} \end{Bmatrix}, \quad \vec{\mathbf{F}}^{\mathrm{v}} = \begin{Bmatrix} \vec{J}_1 \\ \dots \\ \vec{J}_{n_s} \\ \bar{\tau} \\ \bar{\tau}\cdot\vec{u} + \sum_s \vec{J}_s h_s + \vec{q}^{\mathrm{ve}} + \vec{q}^{\mathrm{tr}} \\ \sum_s \vec{J}_s h_s^{\mathrm{ve}} + \vec{q}^{\mathrm{ve}} \end{Bmatrix}, \quad \mathbf{F} = \begin{Bmatrix} \dot{\omega}_1 \\ \dots \\ \dot{\omega_{n_s}} \\ 0 \\ 0 \\ \dot{\Omega} \end{Bmatrix} \tag{2}$$

and ρ is the density of the mixture, ρ_s is the partial density of species s, p is the static pressure, e and e^{ve} are, respectively, the total energy per unit mass and the vibrational energy per unit mass for the mixture, h is the total enthalpy per unit mass, $\vec{J}_s$ is the species mass diffusion flux, $\bar{\tau}$ is the viscous stress tensor, $\vec{q}$ is the conduction heat flux, index s denotes the s^{th} chemical species and n_s is the total number of species.

Calculating the nonequilibrium thermodynamic state and source terms is necessary to close the system of governing equations that describes hypersonic flows. This is achieved by means of coupling with appropriate multi-temperature thermochemistry models. The equations presented below describe the implementation of the two-temperature model for a mixture composed of neutral species, provided by the Mutation++ library [21]. Each individual species s is assumed to behave as an ideal gas. Hence, the total pressure of the mixture p is defined by Dalton's Law as the summation of the partial pressures associated with each species p_s, determined by the ideal gas law,

$$p = \sum_{s=1}^{n_s} p_s = \sum_{s=1}^{n_s} \rho_s \frac{R_{\mathrm{u}}}{M_s} T_{\mathrm{tr}}, \tag{3}$$

where R_{u} is the universal gas constant, M_s is the molar mass of species s and T_{tr} is the trans-rotational temperature. The total specific energy of the flow e is given as the sum of the internal and kinetic energies:

$$e = \sum_{s=1}^{n_s} c_s e_s + \frac{1}{2}u^2, \tag{4}$$

where c_s is the mass fraction of species s, u is the magnitude of the flow velocity vector and e_s is the specific internal energy of the species, given by the sum of the energy of formation and the contribution of each internal mode (t-translational, r-rotational, v-vibrational, e-electronic),

$$e_s = e_s^{\mathrm{t}}(T_{\mathrm{tr}}) + e_s^{\mathrm{r}}(T_{\mathrm{tr}}) + e_s^{\mathrm{v}}(T_{\mathrm{ve}}) + e_s^{\mathrm{e}}(T_{\mathrm{ve}}) + e_s^0. \tag{5}$$

Using a combination of statistical thermodynamics and quantum mechanics, the internal mode energies are defined on the basis of the Rigid-Rotor Harmonic Oscillator model (RRHO) as:

$$e_s^{\mathrm{t}}(T_{\mathrm{tr}}) = \frac{3}{2}\frac{R_{\mathrm{u}}}{M_s}T_{\mathrm{tr}}, \tag{6}$$

$$e_s^{\mathrm{r}}(T_{\mathrm{tr}}) = \begin{cases} \frac{R_{\mathrm{u}}}{M_s}T_{\mathrm{tr}}, & \text{for linear molecules,} \\ 0, & \text{for atoms,} \end{cases} \tag{7}$$

$$e_s^{\mathrm{v}}(T_{\mathrm{ve}}) = \begin{cases} \frac{R_{\mathrm{u}}}{M_s}\sum_v \frac{\theta_{v,s}^{\mathrm{v}}}{\exp(\theta_{v,s}^{\mathrm{v}}/T_{\mathrm{ve}})-1}, & \text{for molecules,} \\ 0, & \text{for atoms,} \end{cases} \tag{8}$$

$$e_s^{\mathrm{e}}(T_{\mathrm{ve}}) = \frac{R_{\mathrm{u}}}{M_s} \frac{\sum_i g_{i,s}\theta_{i,s}^{\mathrm{e}} \exp(-\theta_{i,s}^{\mathrm{e}}/T_{\mathrm{ve}})}{\sum_i g_{i,s} \exp(-\theta_{i,s}^{\mathrm{e}}/T_{\mathrm{ve}})}, \tag{9}$$

where $\theta_{v,s}^{\mathrm{v}}$ is the characteristic vibrational temperature of species s and vibrational mode v, $g_{i,s}$ and $\theta_{i,s}^{\mathrm{e}}$ are the degeneracy and characteristic electronic temperature, respectively, at energy level i for species s. The formation energy e_s^0 is referenced at the standard state conditions of 298.15 K and 1 atm.

The conservation equation for the mass of the mixture is replaced by a mass conservation equation for each species in the gas, incorporating a production/destruction term that results from chemical activity. The chemical source term $\dot{\omega}_s$ is given by

$$\dot{\omega}_s = M_s \sum_{r=1}^{n_r} (\nu''_{s,r} - \nu'_{s,r}) \left[k_{\mathrm{f},r} \prod_{j=1}^{n_s} \hat{\rho}_j^{\nu'_{j,r}} - k_{\mathrm{b},r} \prod_{j=1}^{n_s} \hat{\rho}_j^{\nu''_{j,r}} \right], \tag{10}$$

where n_r and n_s are, respectively, the number of reactions and the number of species, ν'_s is the forward reaction stoichiometry coefficient, ν''_s is the backward reaction stoichiometry coefficient, $\hat{\rho}_j$ is the molar density, $k_{\mathrm{f},r}$ is the forward reaction rate and $k_{\mathrm{b},r}$ is the backward reaction rate. The forward reaction rate for each reaction r is defined according to the modified Arrhenius equation

$$k_{\mathrm{f},r} = A_r T_{\mathrm{c}}^{N_r} \exp\left(-\frac{\theta_r}{T_{\mathrm{c}}}\right), \tag{11}$$

where the coefficients A_r, θ_r and N_r are obtained from experimental data and are, respectively, the reaction rate constant, the activation temperature and an exponent. The backward reaction rates $k_{\mathrm{b},r}$ are determined from the equilibrium reaction rates, $k_{\mathrm{b},r} = k_{\mathrm{f},r}/k_{\mathrm{eq},r}$ for every reaction r. The equilibrium reaction rates $k_{\mathrm{eq},r}$ are determined as a function of the Gibbs free energy. T_{c} is the controlling temperature determined by Park's two-temperature model [22]:

- Dissociation reactions AB + M $\rightleftharpoons$ A + B + M

  $T_{\mathrm{c}} = \sqrt{T_{\mathrm{tr}} T_{\mathrm{ve}}}$ for the forward rate; $T_{\mathrm{c}} = T_{\mathrm{tr}}$ for the backward rate;

- Exchange reactions AB + C $\rightleftharpoons$ A + BC

  $T_{\mathrm{c}} = T_{\mathrm{tr}}$.

In the two-temperature model, the energy transfer mechanisms, that determine the change in vibrational energy of the mixture, are accounted for in the source term vector. The source term $\dot{\Omega}$ is defined as the sum of the vibrational-to-translational energy transfer and energy exchanges due to chemical activity,

$$\dot{\Omega} = \sum_{s=1}^{n_s} \dot{\Omega}_s^{\mathrm{tr:ve}} + \dot{\Omega}_s^{\mathrm{c:v}} + \dot{\Omega}_s^{\mathrm{c:e}}. \tag{12}$$

The term $\dot{\Omega}^{\mathrm{tr:ve}}$ concerns the rate of energy exchange between the translational and vibrational energy modes, following the Landau-Teller model [23]

$$\dot{\Omega}_s^{\mathrm{tr:ve}} = \rho_s \frac{e_s^{\mathrm{ve}}(T_{\mathrm{tr}}) - e_s^{\mathrm{v}}(T_{\mathrm{ve}})}{\tau_s^{\mathrm{V\text{-}T}}}. \tag{13}$$

The vibrational relaxation time of each species, $\tau_s^{\mathrm{V\text{-}T}}$, is given by the Millikan and White empirical formula [24] and the Park correction [25],

$$\tau_s^{\mathrm{V\text{-}T}} = \tau_s^{\mathrm{MW}} + \tau_s^{\mathrm{P}}, \tag{14}$$

where the Millikan and White relaxation time of species s depends on the vibrational relaxation times of the interactions with collision partners r and the corresponding molar fractions X_r, as follows

$$\tau_s^{\mathrm{MW}} = \left(\sum_{r=1}^{n_s} \frac{X_r}{\tau_{s-r}^{\mathrm{MW}}} \right)^{-1}, \tag{15}$$

$$\tau_{s-r}^{\mathrm{MW}} = \exp\left(A_{s,r} \left(T_{\mathrm{tr}}^{-\frac{1}{3}} - B_{s,r} \right) - 18.42 \right) \left(\frac{p}{101325} \right)^{-1} [s]. \tag{16}$$

The Park correction is given by

$$\tau_s^{\mathrm{P}} = \left(N_s \sigma_s \sqrt{\frac{8 R_{\mathrm{u}} T_{\mathrm{tr}}}{\pi M_s}} \right)^{-1}, \tag{17}$$

where r denotes the r^{th} species, X_r is the molar fraction, N_s is the number density and σ_s is an effective cross-section for vibrational relaxation. The change in vibrational-electronic energy of the mixture due to the production/destruction of species is accounted for in the terms $\dot{\Omega}_s^{\mathrm{c:v}}$ and $\dot{\Omega}_s^{\mathrm{c:e}}$, given by

$$\dot{\Omega}_s^{\mathrm{c:v}} = c_1 \dot{\omega}_s e_s^{\mathrm{v}}, \qquad \dot{\Omega}_s^{\mathrm{c:e}} = \dot{\omega}_s e_s^{\mathrm{e}}. \tag{18}$$

Both preferential and non-preferential dissociation models can be considered to account for the coupling between vibrational energy modes and finite-rate chemistry. For the non-preferential dissociation model, which assumes that molecules are destroyed or created at the average vibrational energy of the cell, $c_1 = 1$. For the preferential dissociation model, it is considered that molecules dissociate more easily when vibrationally more excited and therefore must "ladder climb" from lower to higher vibrational states to be dissociated - in this case $c_1 = 0.3$ and $e_s^{\mathrm{v}} = e_{dissociation}$.

With regard to dissipative fluxes, the mass diffusion flux of each species $\vec{J}_s$ is described by Fick's Law of diffusion:

$$\vec{J}_s = \rho_s \vec{V}_s \tag{19}$$

where $\vec{V}_s$ is the element diffusion velocitiy, obtained by solving the Stefan-Maxwell equations under the Ramshaw approximation. The viscous stress tensor is written in vector notation as:

$$\bar{\tau} = \mu \left(\nabla \vec{u} + \nabla \vec{u}^{\mathrm{T}} - \frac{2}{3} \bar{I} (\nabla \cdot \vec{u}) \right) \tag{20}$$

where μ is the mixture viscosity coefficient. The conduction heat flux for each thermal energy mode $\vec{q_k}$ is assumed to be given by Fourier's Law of heat conduction:

$$\vec{q_k} = \lambda_k \vec{\nabla}(T_k) \tag{21}$$

where T_k is the temperature and λ_k is the thermal conductivity coefficient of the kth energy mode. The mixture viscosity μ and thermal conductivity λ_k coefficients are determined by Wilke's mixing rule [26], with pure species properties determined from accurate collision integral data.

B. Equilibrium thermally perfect gas model (TPG)

The system of equations implemented for the thermally perfect gas model follows the widely known classical Navier-Stokes approach for a continuum, viscous laminar, frozen flow in thermal equilibrium, with a single equation for the energy (total energy of the mixture) and assuming a single temperature T. The specific heats are defined as:

$$C_p = \frac{\gamma R}{\gamma - 1}, \tag{22}$$

$$C_v = C_p - R, \tag{23}$$

where C_p is the specific heat of the mixture at constant pressure, C_v is the specific heat of the mixture at constant volume, $\gamma = \frac{C_p}{C_v}$ is the ratio of specific heats and R is the gas constant of the mixture. The thermally perfect gas model considers the impact of vibrational relaxation implicitly and in a simplified manner. As the internal energy of the gas increases, a

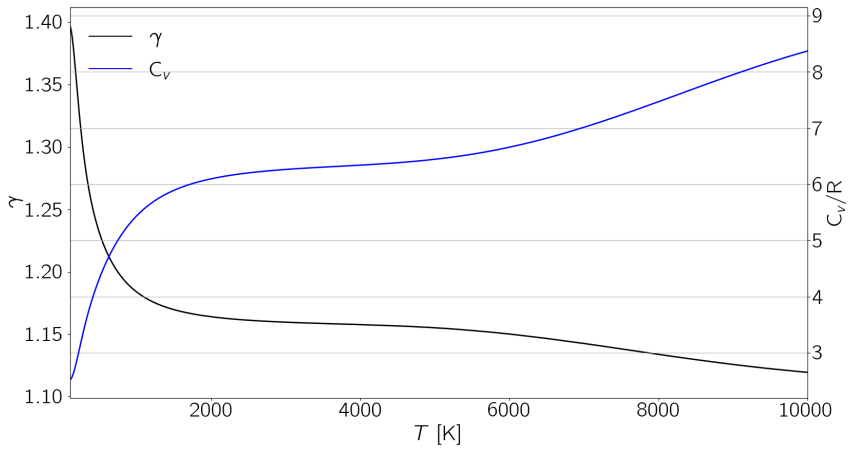

Fig. 1 Variation of specific heat at constant volume C_v and specific heat ratio γ of a CO_2:0.97, N_2:0.03 mixture with temperature for a thermally perfect gas model.

portion of it activates the vibrational modes instead of raising the temperature of the gas. The two-temperature model introduced in the previous section accounts for the relaxation time that it takes for this process to reach a state of equilibrium through the presence of the source term that models the energy transfer between translational/rotational mode and vibrational/electronic mode (equation 13). The thermally perfect gas model also accounts for the energy redistribution between these two modes, however it considers that the process occurs instantaneously, i.e., the flow is assumed to always be in thermal equilibrium and only one temperature is considered. The distribution of energy between trans-rotational and vibro-electronic modes is modelled by a change of specific heats as function of the temperature $C_p = f(T)$ and $C_v = f(T)$. The change of thermodynamic properties with temperature and the value of temperature for which this process becomes significant depend on the characteristic vibrational temperature of the molecules and therefore on the mixture in question. As shown in Fig. 1, for the mixture studied in this work, this model predicts a significant decrease of the specific heat ratio for temperatures up to 1000 K, above which this change becomes more gradual. The overall decrease of specific heat ratio as well as the evolution of C_v with temperature - i.e. the fact that C_v increases linearly with T for lower temperatures and for $T >$ 1000 K the impact of the temperature increase becomes smaller - is a reflection of the fact that part of the internal energy of a molecule is used to excite the vibrational degrees of freedom instead of raising the temperature of the gas. The graph shows that the low characteristic vibrational temperature of CO_2 molecules has a very significant impact on the thermodynamic properties of the mixture.

III. SU2-NEMO solver, Mutation++ library and AMG mesh adaptation library

The open-source SU2 software suite* [15], written in C++ and Python, is the basis for this study. It is built specifically for the analysis of partial differential equations (PDEs) and PDE-constrained optimization problems with state-of-the-art numerical methods. The solver is rapidly establishing itself within the open-source community as a prominent software for multiphysics analysis and design, including the simulation of chemically-reactive and nonequilibrium flows [27] with the development of SU2-NEMO (NonEquilibrium MOdels solver). Extensive validation of the software is reported in the literature [14, 15]. The-closure-of the governing equations for the system that describes hypersonic flows is achieved by means of coupling with appropriate thermochemistry models (presented in Section II.A). To this purpose, SU2-NEMO is coupled to the Mutation++ library† [21] (Multicomponent Thermodynamic And Transport properties for IONized gases in C++), that provides efficient algorithms for the computation of thermodynamic, transport (viscosity, thermal conductivity and diffusion) and chemical kinetic gas properties. The library has been designed for robustness over a wide range of temperatures and its accuracy in dealing with multi-temperature models, with the following constraints in mind: 1) high fidelity of the physical models, ensuring that the laws of thermodynamics are satisfied and that results are validated against existing experimental data, 2) low computational cost, 3) a modern, object-oriented, extensible framework, and 4) detailed in-source and user's guide documentation in order to facilitate model improvement

*https://github.com/su2code/SU2
†https://github.com/mutationpp/Mutationpp

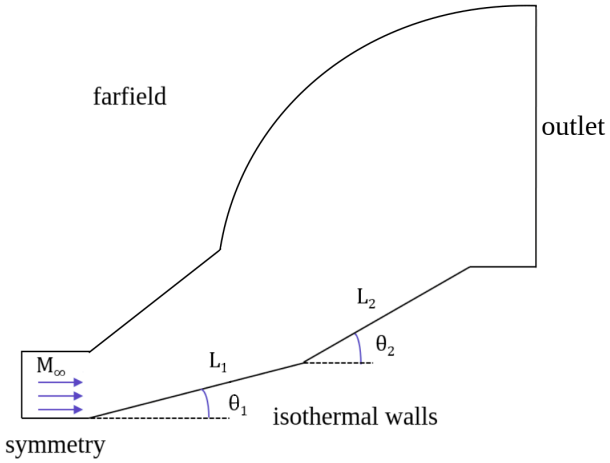

Fig. 2 Double-wedge geometry, computational domain and boundary conditions.

and collaboration. The library has been extensively validated as a software on its own [21] and some validation work has been carried out for the coupling of Mutation++ with the SU2-NEMO solver [14].

To ensure that all the complex flow structures are accurately predicted while minimizing computational costs, mesh adaptation tools are used in this work. For the cases where the flow is steady, anisotropic adaptation with the pyAMG library is adopted to capture the high-gradient localized steady features. The library was developed by INRIA [‡] [28–31] to be a fast, robust and automatic tool that performs anisotropic mesh adaptation for complex geometries generating multi-scale and multi-direction phenomena in the flowfield (shock waves, contact discontinuities, boundary layers, turbulence, etc.). It is a metric-based mesh generation tool that creates highly anisotropic meshes by enforcing the alignment of the element edges with the flow features. Successive local mesh modifications such as edge collapse, point insertion, edge swapping and point smoothing are performed until the output mesh meets the metric requirements, as well as some mesh quality constraints to ensure the stability and enhance the performance of the CFD solver. The Mach number is used as variable for the error estimation used in the adaptation process. This choice is based on the fact that all relevant flow features (shocks, expansions, contact discontinuities, boundary layer, separations, vortexes) translate to Mach number gradient, therefore guaranteeing that all of them are be captured appropriately.

IV. Results and discussion

In this section, a numerical study of shock interaction mechanisms in a CO_2-dominated flow over a double-wedge geometry, illustrated in Fig. 2, is reported. The interference of different shock waves typically generated in a flow over this type of geometry leads to complex flow features that can result in extremely localized and intense peaks of pressure and heat flux along the surface. The leading shock wave generated at the beginning of the first wedge intersects the separation shock caused by the re-circulation bubble occurring in the compression corner. The flow physics typically occurring in the compression corner is depicted in Fig. 3. As shown in this figure, besides the presence of a shock wave due to boundary layer separation, re-attachment of the boundary layer leads to a compression wave that may converge into another shock. Depending on the considered freestream conditions, gas mixture and angles of each wedge, the flow physics resulting from the interference of the various features will result in different shock interaction mechanisms.

In this study, two different geometries are considered: a 15°-40°and a 15°-50°double-wedge. For both cases, $L_1 = L_2 = 0.2$ m. The computational domain and boundary conditions are shown in Figure 2: for the most left horizontal segment a symmetry boundary condition is applied; the surfaces are chosen to be viscous isothermal walls; an outlet boundary condition is chosen for the exit and farfield is considered for the remaining boundaries. Numerical simulations are performed for a flow of CO_2:97%, N_2:3% referring to the atmosphere of Mars. Simulation parameters, presented in Table 1, are chosen so that the freestream conditions are in the laminar continuum regime and values of pressure and temperature consistent with the Martian atmosphere. The freestream flow is considered to be in thermal equilibrium. For the conditions studied, the flow is chemically frozen but in thermal nonequilibrium. Two different

[‡]https://pyamg.saclay.inria.fr/

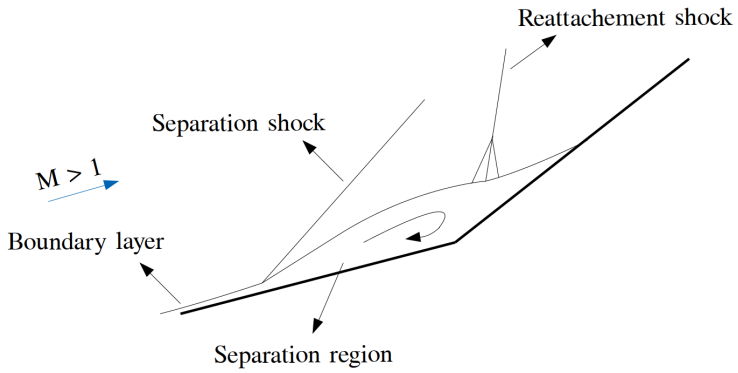

Fig. 3 Compression corner re-circulation bubble and shock wave system.

ways of modelling the effect of vibrational relaxation are employed as per Section II.B. For simplicity, hereinafter the thermally perfect gas model is referred to as TPG and the two-temperature model as NEQ. Both qualitative and quantitative comparisons are reported to assess the impact of the different models on the characteristics of the flow in terms of shock structures as well as surface pressure and wall heat flux distribution, respectively.

Table 1 Simulation parameters.

M_∞	p_∞ [Pa]	T_∞ [K]	T_{wall} [K]	Mole fractions
9	10	160	300	CO_2: 0.97 N_2: 0.03

A. Mesh adaptation and grid convergence

As previously discussed, the flow physics encountered in this type of flows is rather complex, including features such as shock waves, boundary layer, contact discontinuities, etc. These features are very localized, highly directional and characterized by sharp gradients. Moreover, they usually separate regions of nearly uniform flow. To guarantee that there is minimum computational waste in accurately capturing shock interaction mechanisms, automatic anisotropic mesh adaptation is used to generate meshes. Anisotropic meshes allow for a clustering of nodes and stretching of the elements in such a way that no significant increase in number of nodes is necessary to improve the accuracy of the solution. The Mach number is chosen as a variable to compute the metric field used for adaptation since all the flow features translate to Mach number gradient and are therefore recognized by the adaptation process. Grid convergence is assessed qualitatively, on the basis of the establishment of a given shock interaction pattern, and quantitatively, by comparing normalized wall surface pressure, wall surface heat flux and the normalized temperature profile normal to the wall at two given locations where relevant flow features are present. A grid convergence study was performed for all test-cases, but for simplicity, only the case of the 15°-50°double-wedge with the TPG model is showcased here. A representation of the original hybrid mesh used for all test-cases is shown at the left side of Fig. 4 and the final adapted mesh for the case of the 15°-50°double-wedge with the TPG model is shown at the right. The two red lines 1 and 2 indicate the positions along the surface of each wedge where the temperature profile normal to the wall is evaluated. Quantitative comparisons for the different levels of adaptation are shown in Fig. 5. Results obtained for levels 2 and 3 are almost identical proving grid convergence. Table 2 reports the number of nodes and elements for the different levels adaptation of all test-cases.

B. Influence of the vibrational relaxation model on the shock interaction patterns

Figures 6 and 7 show the obtained numerical results for the 15°-40°double-wedge case. Figure 6 shows contours of temperature for the TPG model and contours of translational and vibrational temperature for the NEQ model. Figure 7 shows contours of pressure for the two models and, at the right, the difference between translational and vibrational temperatures of the NEQ model, to provide a measure of the thermal nonequilibrium occurring in the flowfield. Figure 8

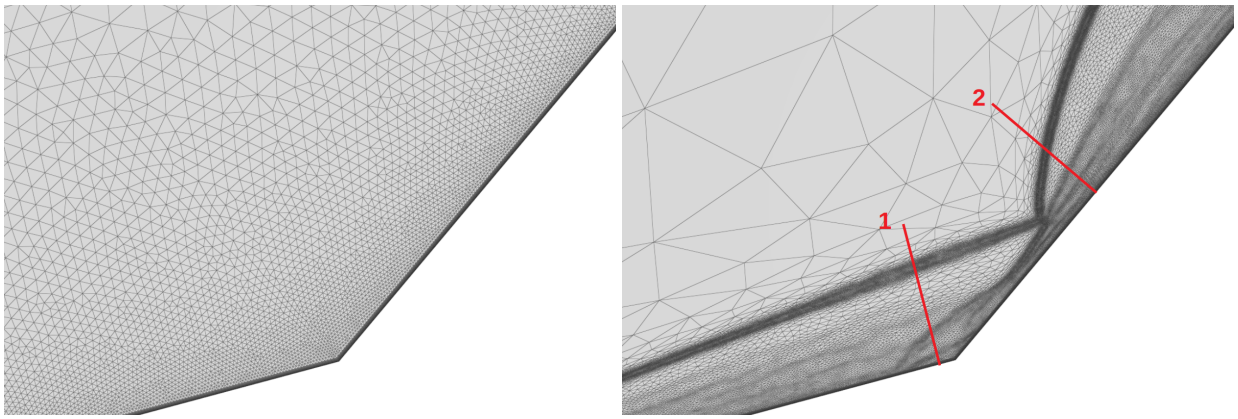

Fig. 4 Original and final hybrid adaptated grid for the 15°-50° TPG test-case. Close-up near the compression corner.

Table 2 Grid convergence study - number of nodes for each grid.

	Level 0	Level 1	Level 2	Level 3
15°-40° TPG	84238	731056	565197	544868
15°-40° NEQ	88251	467418	475209	507297
15°-50° TPG	83594	485268	461541	448061
15°-50° NEQ	85143	412671	416618	422547

shows a schematic of the shock interaction pattern obtained for the two models, to help describing and understanding the system of waves observed. For both models, an Edney type VI pattern is observed [1], characterized by the interaction of two oblique shocks at an intersection point P, from which another shock CS, a contact discontinuity CD and an expansion wave EW, reflected on the surface of the second wedge, are generated. However, different shock interaction mechanisms are obtained for the two models, and these differences arise from the different size of the separation bubble occurring in the compression corner, and the resulting behaviour of the shock system that is generated in this region. The boundary layer is significantly thicker for the NEQ model. This is due to a stronger deceleration of the flow across the first oblique shock LS. The NEQ model results in a stronger LS shock (it was confirmed that the angle of this shock is smaller in the case of the TPG model) because of the relaxation time that it takes for the flow to reach a state of equilibrium. Right behind the shock wave, vibrational levels are not populated instantaneously in the case of the NEQ model, which means that the portion of kinetic energy of the flow that is transformed into internal energy across the shock will be stored only in the trans-rotational degrees of freedom.

In the TPG model, on the contrary, the same portion of energy is redistributed instantaneously amongst the trans-rotational and vibro-electronic modes, which means that, to deflect in the same direction, the flow does not decelerate as much as in the case of the NEQ model. Accordingly, the translational temperature of the NEQ model is overall higher than the temperature of the TPG model (this is more evident behind shock CS, with green regions for the former model and red regions for the latter). Additionally, the differences between translational temperature and vibrational temperature of the NEQ model (shown in Fig. 7) confirm that the flowfield is in thermal nonequilibrium, with translational energy larger than vibrational energy everywhere ($T_{tr} > T_{ve}$). For every point in the flow, the TPG model is under-predicting the time that it takes for the redistribution of energy to occur between the two modes of energy considered in the two-temperature model. The thicker boundary layer in the NEQ model leads to an earlier separation and significantly larger separation bubble relative to the TPG model. The shock interaction mechanism in the NEQ case is characterized by a detachment shock DS (region of dark purple to blue in the pressure contours) generated as a result of the separation and, downstream, a series of compression waves (gradient light blue/green/yellow/red near the surface, in the pressure contours) that converge into a re-attachment shock RS where the flow deflects to re-attach the boundary

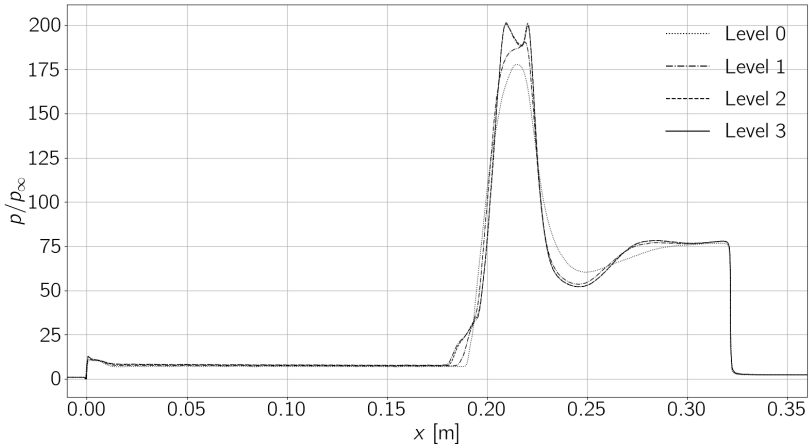

(a) Normalized surface pressure profile.

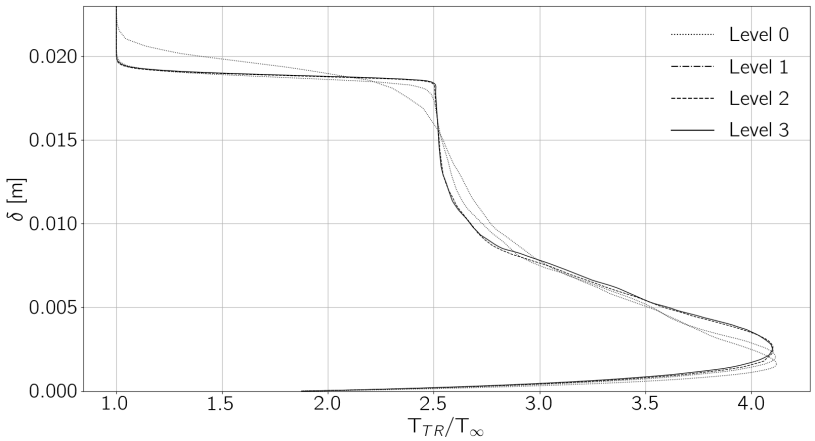

(b) Normalized temperature in location 1.

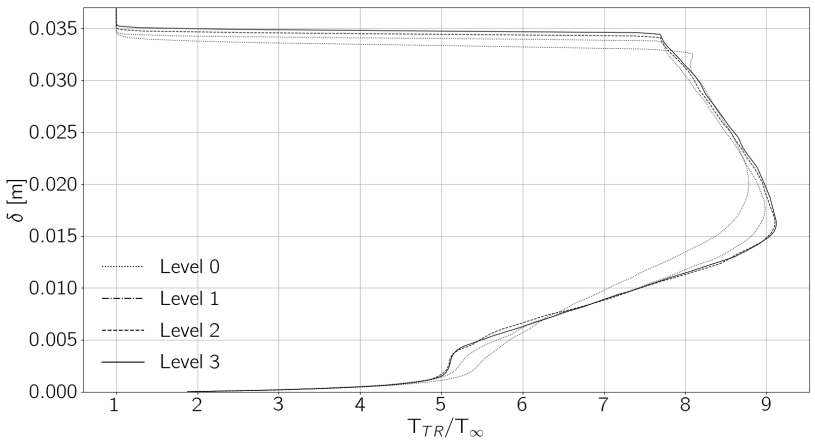

(c) Normalized temperature in location 2.

Fig. 5 Grid convergence study for the case of the 15-°-50°double-wedge with TPG model.

layer. The separation bubble also occurs in the case of the TPG model but can not be visualized in these plots due to its very small size. In this case, the series of compression waves resulting from the re-attachment of the boundary layer simply converges into the detachment shock DS and no re-attachment shock is observed . This is the main difference between the shock interaction mechanisms observed for this geometry using the two different models to account for vibrational excitation.

When it comes to surface loads, it can be seen in Fig. 9, at the right, that the intensity of the pressure peaks is almost identical for the models. Moreover, it is evident that this peak occurs downstream of the compression resulting from the boundary layer re-attachment. It occurs later for the case of the NEQ model due to the larger size of the separation bubble. The location of the heat flux peaks along the surface of the second wedge fairly correspond to the ones of the peaks of pressure. In terms of intensity, the TPG model results in an approximately 15% larger value of the peak heat flux.

Figures 10 and 11 show the obtained numerical results for the 15°-50°double-wedge case, following the same set of results that was presented for the 15°-40°double-wedge. Figure 12 shows a schematic of the shock interaction pattern obtained for the two models, to help describing and understanding the system of waves observed. Both resulting shock structures are typical of an Edney type V interaction [1], characterized by a triple-point P, where an oblique shock intersects with the bow shock, and from which a transmitted shock TS emerges in a Mach reflection structure. The latter shock interacts with another oblique shock, leading to a reflection of two shock waves from opposite families, which is one of the key features in the type V six-shock interaction. Similarly to what was observed for the previous test-case, the interaction of this system of waves with the flow features generated in the vicinity of the separation bubble leads to overall different shock interaction mechanisms for the two models TPG and NEQ. Following the reasoning explained previously about the impact of enforcing instantaneous thermal equilibrium (TPG model) vs. vibrational excitation associated to a given relaxation time (NEQ), the thicker boundary layer occurring for the latter model leads to a significantly larger separation region.

In the case of the TPG model, the detachment shock DS directly interacts with the reattachment shock RS, leading to the contact discontinuity CD1. The regular reflection of the transmitted shock TS and the detachment shock DS gives rise to the reflected shocks RS1 and RS2, respectively. Shock RS2 impinges on the surface of the second wedge and shock RS1 reflects on the contact discontinuity CD2 emanating from the triple point P and turns it upward. This reflection results in the expansion wave EW that reflects on the surface of the second wedge downstream of RS2 (contour gradient red/yellow/green/light blue near the surface of the second wedge in Figure 11).

For the case of the NEQ model, the detachment shock DS (region of purple to dark purple in Fig. 11) occurs earlier and has a larger angle than for the previous model. As a consequence, this shock interacts with the nose leading shock LS in what can be considered a local Edney type VI interaction [1] without the typical expansion wave (observed for example in the two test-cases of the 15°-40°geometry), since from the intersection point Q a contact discontinuity CD1 (separating regions of dark and light blue in Fig. 10) and a shock CS are generated. The series of compression waves caused by the re-attachment of the boundary layer converge in a shock wave RS (separating regions of dark purple and red in Fig. 11) that interacts with the contact discontinuity CD1, turning it upwards. A portion of shock RS is reflected on the contact discontinuity CD1 as the expansion wave EW1. Shock CS2 generated at the intersection point S interacts with the transmitted shock TS, from which the reflected shocks RS1 and RS2 emerge. Shock RS2 interacts with the contact discontinuity CD1 generating shock RS3 that impinges on the surface of the second wedge. Unlike the case of the 15°-40°double-wedge, there is a significant portion of the domain where vibrational excitation relaxes up to a state of thermal equilibrium, as shown in white contours in Fig. 11 at the right.

The surface pressure profile of the 15°-50°double-wedge exhibits two peaks of pressure for both models, the one on the left side resulting from the re-attachment compression and the second one due to shock impingement on the surface (referring to Fig. 9). It is interesting to notice that for the TPG model the two peaks have a similar intensity, whereas in the NEQ model the re-attachment pressure peak is about 12% larger than the one due to impingement. This is due to the different shock structures obtained for each model: for the TPG gas, the reattachment and impinging shocks have a similar angle, as opposed to the case of the NEQ gas, for which the reattachment shock is stronger. The higher peak of pressure of the NEQ model is about 16 % smaller than the one obtained for the TPG model. Given the explanation mentioned previously for the specifics of the different modelling and its impact on the flow features, it could be somewhat expected that the overall stronger shocks in the NEQ would also result in larger pressure peaks. However, the different flow features that characterize the shock structures of each model lead to a weaker compression on the surface for both peaks. Furthermore, the differences in the size of the separation bubble are also evident in the pressure plot, with boundary layer detachment occurring at approximately $x = 0.125$ m for the NEQ model and at $x = 0.18$ m for the TPG model. Similar to the surface pressure, the heat flux distribution exhibits two peaks, corresponding to the

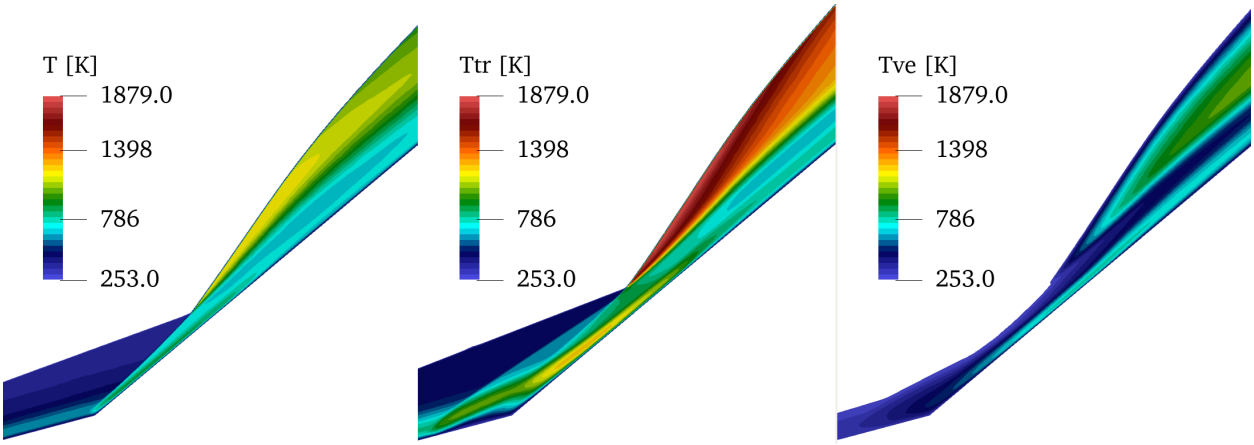

Fig. 6 Temperature contours of the 15°-40°double-wedge flow: TPG (left) and NEQ (right) models.

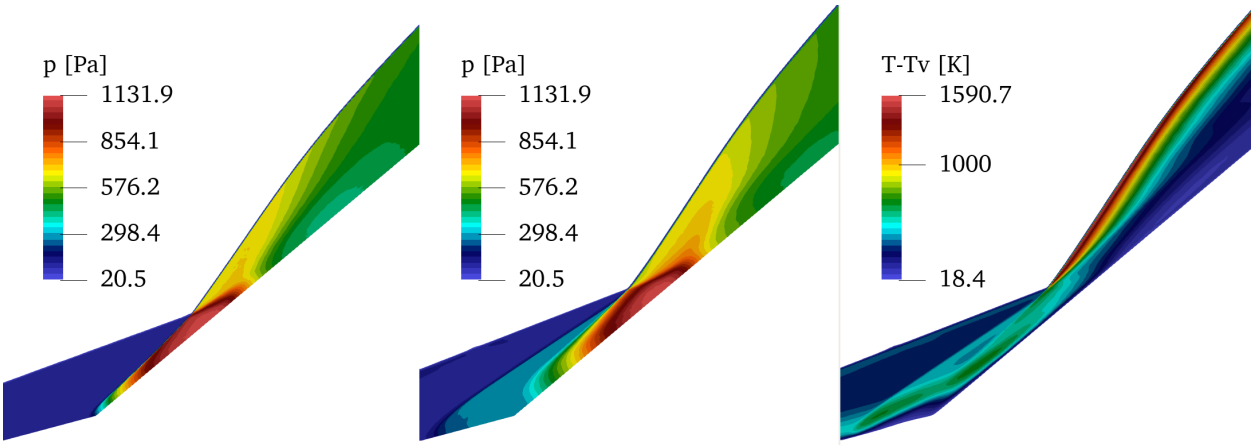

Fig. 7 Pressure contours of the 15°-40°double-wedge flow: TPG (left) and NEQ (right) models.

re-attachment and shock impingement regions. It shows a similar trend of the one observed for the 15°-40°case, with larger and earlier peaks for the TPG model. As expected from increasing the angle of the second wedge, the peak of heat flux is larger for the 15°-50°case despite the model used.

V. Conclusions

A numerical study on thermal nonequilibrium CO_2-dominated flows has been carried out to investigate viscous shock interaction mechanisms and the influence of different assumptions for the intra-molecular energy transfer processes. Two different geometries, a 15°-40°and a 15°-50°double-wedge, have been used as test cases to study the interference of flow features generated due to shock-shock and shock-boundary layer interaction and behaviour of resulting pressure and heat flux loads on the surface. Two different assumptions are considered to model the high-temperature effect of excitation of vibrational degrees of freedom of the polyatomic molecule and the subsequent partitioning of internal energy amongst the various internal energy modes: a) the more detailed two-temperature model accounts for the relaxation time that it takes to equilibrate the energy transfer between the trans-rotational and the vibro-electronic modes, whereas b) the thermally perfect gas model assumes an instantaneous energy redistribution process, therefore enforcing thermal equilibrium.

For each geometry, the shock structures obtained further from the wall corresponded to the same type of interaction. An type VI interaction is obtained for the 15°-40°case and a type V regular shock reflection is obtained for the 15°-50°case. However, the consideration of finite-rate redistribution of internal energy in the nonequilibrium model results in a stronger deceleration of the flow across the nose oblique shock wave, leading to a thicker boundary layer and

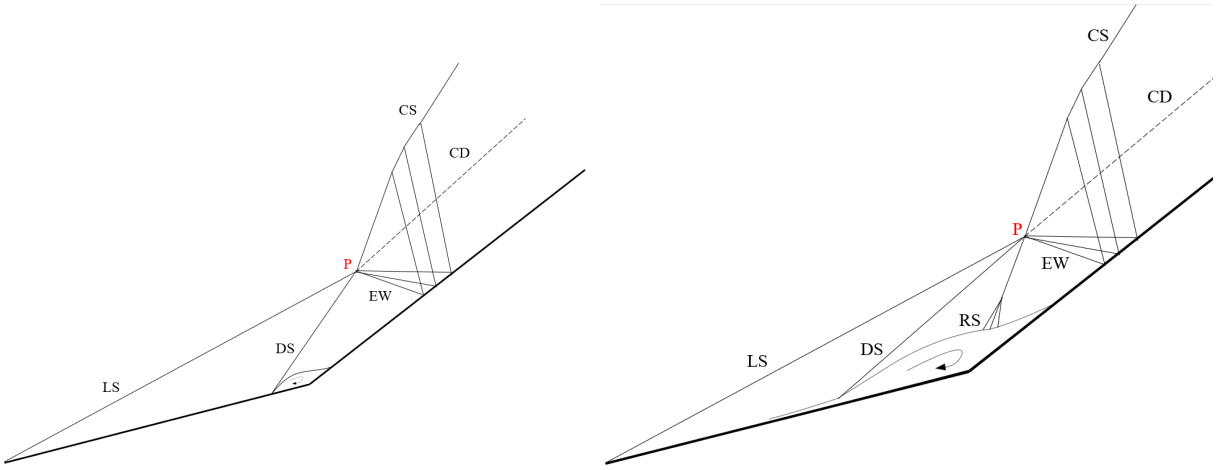

Fig. 8 Schematic of shock interaction patterns obtain for the 14°-40°double wedge: TPG (left) and NEQ (right) models

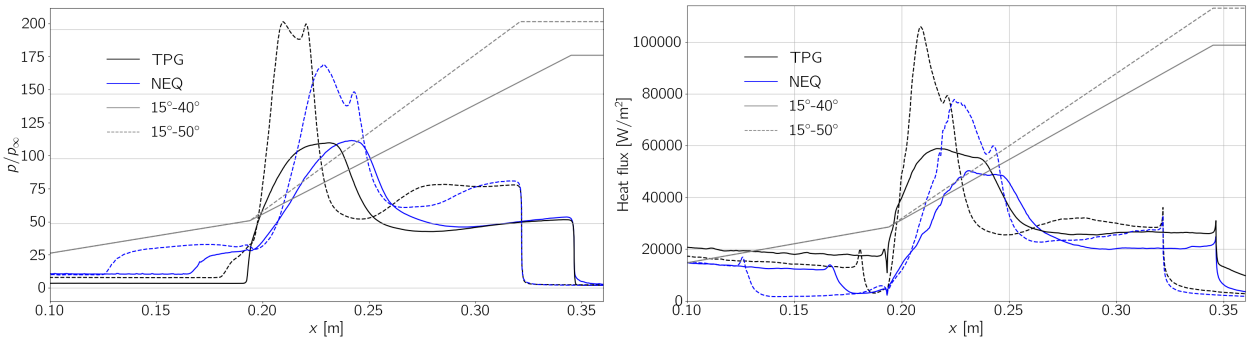

Fig. 9 Normalized surface pressure profiles (left) and heat flux distributions (right).

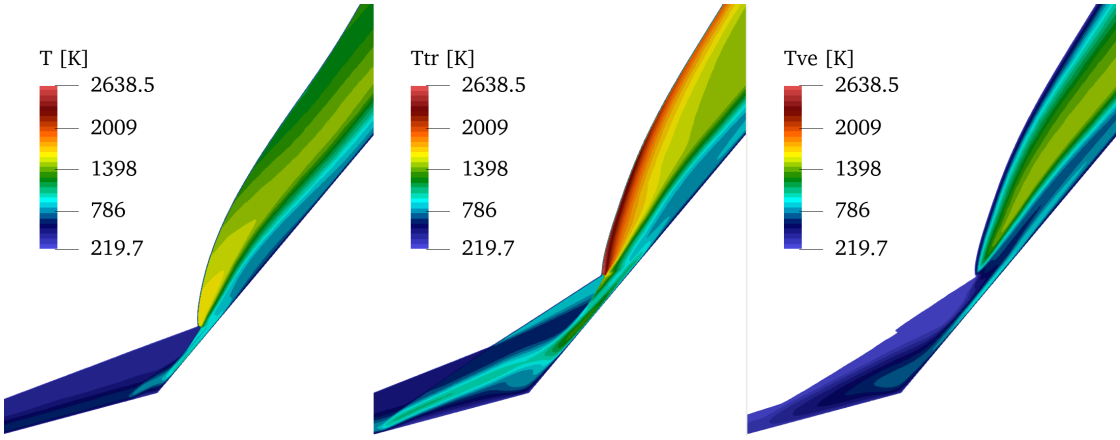

Fig. 10 Temperature contours of the 15°-50°double-wedge flow: TPG (left) and NEQ (right) models.

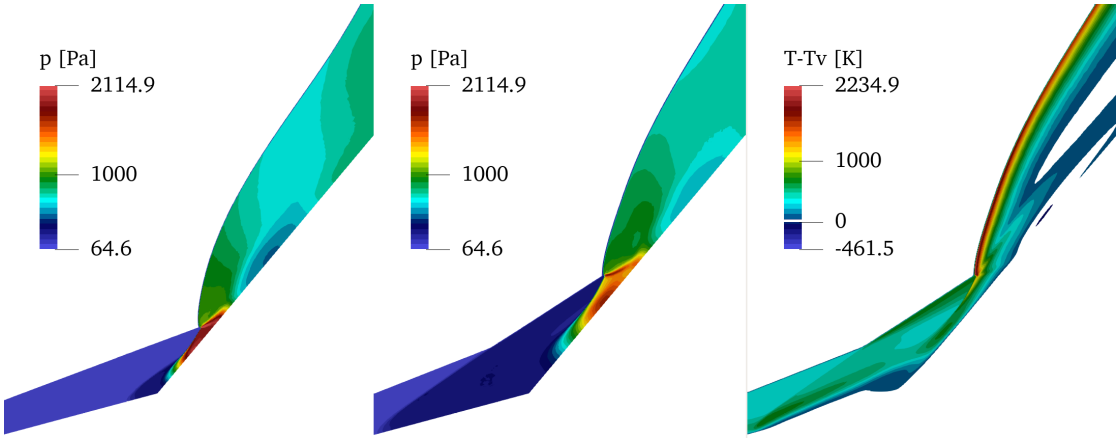

Fig. 11 Pressure contours of the 15°-50°double-wedge flow: TPG (left) and NEQ (right) models.

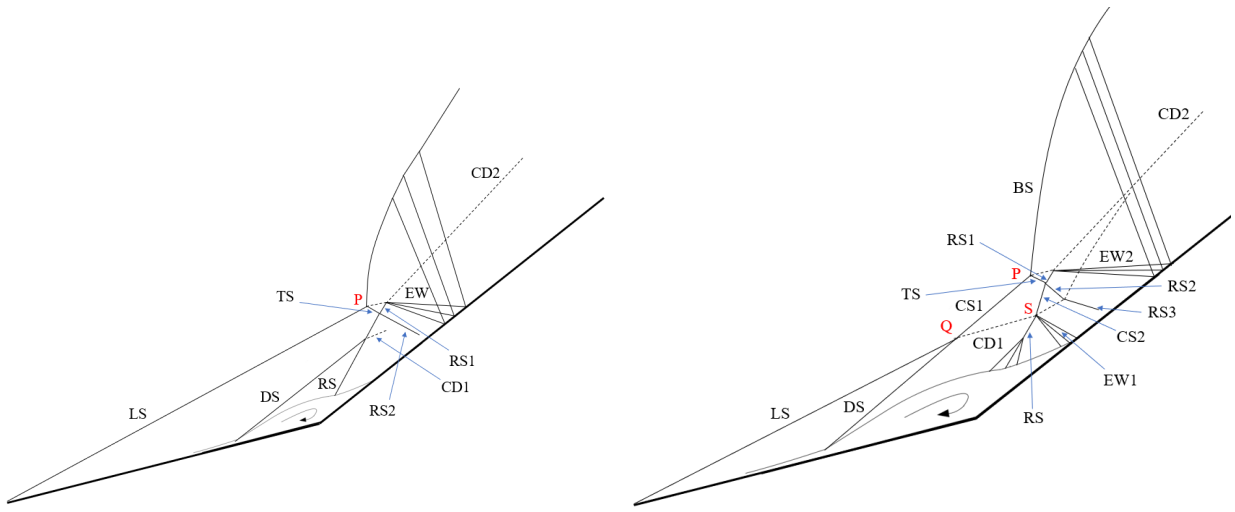

Fig. 12 Schematic of shock interaction patterns obtain for the 15°-50°double wedge: TPG (left) and NEQ (right) models

significantly larger separation bubble. In both cases, the different sizes of the compression corner separation bubble generated different systems of waves in this region, causing the overall shock interaction patterns to differ as well. Aerothermal loads are equally affected by the physical model. Different locations of pressure and heat flux peaks are obtained for each model. In the case of the lower aft wedge angle, the intensity of the peaks is not much affected by the different physical assumptions, as opposed to the 15°-50°double-wedge, for which larger peaks are obtained for the thermally perfect gas model. Despite the fast vibrational relaxation of the CO_2 modes and the presence of thermal equilibrium regions in the case of the higher aft wedge angle, the oversimplifying assumptions of the thermally perfect gas model greatly influence the flow macroscopic properties, the obtained flow features and overall shock interaction mechanism.

Acknowledgments

The authors wish to acknowledge the support of the EPSRC funded ARCHIE-WeSt High Performance Computer (www.archie-west.ac.uk), EPSRC grant no. EP/K000586/1. Further, the authors acknowledge the contributions of James B. Scoggins from CMAP, at Ècole Polytechnique, Route de Saclay, 91128 Palaiseau, France and Walter T. Maier from Stanford University, Stanford, CA 94305, U.S.A.

References

[1] Edney, B., "Anomalous Heat Transfer and Pressure Distributions on Blunt Bodies at Hypersonic Speeds in the Presence of an Impinging Shock," 1968. Report 115. Flygtekniska Foroksanstalten, Stockholm: The Aeronautical Research Institute of Sweden.

[2] Olejniczak, J., Wright, M., and Candler, G., "Numerical study of inviscid shock interactions on double-wedge geometries," *Journal of Fluid Mechanics*, Vol. 352, 1997, pp. 1–25. doi:10.1017/S0022112097007131.

[3] Halder, P., Sinhamahapatra, K. P., and Singh, N., "Type-VI and Type-V Shock-Shock Interactions on Double-Wedge Geometries Using AUSM+ on Unstructured Grid," *International Journal of Hypersonics*, Vol. 1, 2010, pp. 225–244. doi:10.1260/1759-3107.1.4.225.

[4] Hu, Z. M., Myong, R. S., Yang, Y. R., and Cho, T. H., "Reconsideration of inviscid shock interactions and transition phenomena on double-wedge geometries in a M_∞=9 hypersonic flow," *Theoretical and Computational Fluid Dynamics*, Vol. 24, No. 6, 2010, pp. 551–564. doi:10.1007/s00162-010-0188-4.

[5] Ben-Dor, G., Vasilev, E. I., Elperin, T., and Zenovich, A. V., "Self-induced oscillations in the shock wave flow pattern formed in a stationary supersonic flow over a double wedge," *Physics of Fluids*, Vol. 15, No. 12, 2003, pp. L85–L88. doi:10.1063/1.1625646.

[6] Badr, M. A., and Knight, D. D., "Shock Wave Laminar Boundary Layer Interaction Over a Double Wedge in a High Mach Number Flow," 52nd Aerospace Sciences Meeting. doi:10.2514/6.2014-1136.

[7] Hu, Z., Myong, R., and Cho, T., "Numerical study of shock interactions in viscous, hypersonic flows over double-wedge geometries," *Shock Waves*, edited by K. Hannemann and F. Seiler, Springer Berlin Heidelberg, Berlin, Heidelberg, 2009, pp. 671–676. doi:10.1007/978-3-540-85168-4_108.

[8] Olejniczak, J., Wright, M., and Candler, G., "Numerical study of shock interactions on double-wedge geometries," 34th Aerospace Sciences Meeting and Exhibit, Reno, NV, 1996. doi:https://doi.org/10.2514/6.1996-41.

[9] Tchuen, G., Fogue, M., Burtschell, Y., Zeitoun, D., and Ben-Dor, G., "Shock-on-shock interactions over double-wedges: comparison between inviscid, viscous and nonequilibrium hypersonic flow," *Shock Waves*, edited by K. Hannemann and F. Seiler, Springer Berlin Heidelberg, Berlin, Heidelberg, 2009, pp. 1497–1502. doi:10.1007/978-3-540-85181-3_114.

[10] Tchuen, G., Burtschell, Y., and Zeitoun, D. E., "Numerical study of the interaction of type IVr around a double-wedge in hypersonic flow," *Computers Fluids*, Vol. 50, No. 1, 2011, pp. 147 – 154. doi:10.1016/j.compfluid.2011.07.002".

[11] Candler, G., *Computation of thermo-chemical nonequilibrium Martian atmospheric entry flows*, 5th Joint Thermophysics and Heat Transfer Conference, ???? doi:10.2514/6.1990-1695.

[12] Park, C., Howe, J. T., Jaffe, R. L., and Candler, G. V., "Review of chemical-kinetic problems of future NASA missions, II: Mars entries," *Journal of Thermophysics and Heat Transfer*, Vol. 8, No. 1, 1994, pp. 9–23. doi:10.2514/3.496.

[13] Windisch, C., Reinartz, B. U., and Müller, S., "Investigation of Unsteady Edney Type IV and VII Shock-Shock Interactions," *AIAA Journal*, Vol. 54, No. 6, 2016, pp. 1846–1861. doi:10.2514/1.J054298.

[14] Garbacz, C., Maier, W., Scoggins, J., Economon, T. D., Magin, T., Alonso, J. J., and Fossati, M., "Shock interactions in inviscid air and CO_2-N_2 flows in thermochemical non-equilibrium," *Shock Waves*, 2021. doi:10.1007/s00193-021-00999-8.

[15] Economon, T. D., Palacios, F., Copeland, S. R., Lukaczyk, T. W., and Alonso, J. J., "SU2: An Open-Source Suite for Multiphysics Simulation and Design," *AIAA Journal*, Vol. 54, No. 3, 2016, pp. 828–846. doi:10.2514/1.J053813.

[16] Gnoffo, P., Gupta, R., and Shinn, J., "Conservation equations and physical models for hypersonic air flows in thermal and chemical nonequilibrium," NASA Technical Paper 2867, 1989, p.158.

[17] Park, C., "Review of chemical-kinetic problems of future NASA missions. I - Earth entries," *Journal of Thermophysics and Heat Transfer*, Vol. 7, No. 3, 1993, pp. 385–398. doi:10.2514/3.431.

[18] Liao, D., Liu, S., Huang, J., Jian, H., Xie, A., and Wang, Z., "Measurement and numerical simulation of shock standoff distances over hypersonic spheres in CO_2 in a ballistic range," *Shock Waves*, Vol. 30, 2020, p. 131–138. doi:10.1007/s00193-019-00923-1.

[19] Armenise, I., Reynier, P., and Kustova, E., "Advanced Models for Vibrational and Chemical Kinetics Applied to Mars Entry Aerothermodynamics," *Journal of Thermophysics and Heat Transfer*, Vol. 30, No. 4, 2016, pp. 705–720. doi:10.2514/1.T4708.

[20] Camac, M., "CO_2 Relaxation Processes in Shock Waves," *Fundamental Phenomena in Hypersonic Flow*, Cornell U.P., Ithaca, N.Y. 1966, pp. 195–215.

[21] Scoggins, J. B., Leroy, V., Bellas-Chatzigeorgis, G., Dias, B., and Magin, T. E., "Mutation++: MUlticomponent Thermodynamic And Transport properties for IONized gases in C++," *SoftwareX*, Vol. 12, 2020, p. 100575. doi:https://doi.org/10.1016/j.softx.2020.100575.

[22] Park, C., "Assessment of two-temperature kinetic model for ionizing air," *Journal of Thermophysics and Heat Transfer*, Vol. 3, No. 3, 1989, pp. 233–244. doi:10.2514/3.28771.

[23] Landau, L., and Teller, E., "Systematics of Vibrational Relaxation," *Physik Zeitschrift der Sowjetunion*, Vol. 10, 1936, pp. 34–38.

[24] Millikan, R. C., and White, D. R., "Systematics of Vibrational Relaxation," *The Journal of Chemical Physics*, Vol. 39, No. 12, 1963, pp. 3209–3213. doi:10.1063/1.1734182.

[25] Park, C., "Assessment of two-temperature kinetic model for ionizing air," *Journal of Thermophysics and Heat Transfer*, Vol. 3, No. 3, 1989, pp. 233–244. doi:10.2514/3.28771.

[26] Wilke, C. R., "A Viscosity Equation for Gas Mixtures," *The Journal of Chemical Physics*, Vol. 18, No. 4, 1950, pp. 517–519. doi:10.1063/1.1747673.

[27] Palacios, F., Copeland, S., Lonkar, A., and Alonso, J., "Adjoint-Based Goal-Oriented Mesh Adaptation for Nonequilibrium Hypersonic Flows," 51st AIAA Aerospace Sciences Meeting including the New Horizons Forum and Aerospace Exposition, Grapevine, TX. AIAA Paper 2013-0552 (2013). doi:10.2514/6.2013-552.

[28] Loseille, A., and Loehner, R., "Boundary Layer Mesh Generation and Adaptivity," 2011. doi:10.2514/6.2011-894.

[29] Loseille, A., and Menier, V., "Serial and Parallel Mesh Modification Through a Unique Cavity-Based Primitive," *Proceedings of the 22nd International Meshing Roundtable*, edited by J. Sarrate and M. Staten, Springer International Publishing, Cham, 2014, pp. 541–558. doi:10.1007/978-3-319-02335-9_30.

[30] Loseille, A., Menier, V., and Alauzet, F., "Parallel Generation of Large-size Adapted Meshes," *Procedia Engineering*, Vol. 124, 2015, pp. 57 – 69. doi:10.1016/j.proeng.2015.10.122, 24th International Meshing Roundtable.

[31] Loseille, A., "Unstructured Mesh Generation and Adaptation," *Handbook of Numerical Methods for Hyperbolic Problems - Applied and Modern Issues*, edited by R. Abgrall and C.-W. Shu, Elsevier, 2017, pp. 263–302. doi:10.1016/bs.hna.2016.10.004.